Journal of Materials Chemistry A

Optimizing Electron Density of Nickel Sulfides Electrocatalysts through Sulfur Vacancy Engineering for Alkaline Hydrogen Evolution

Journal:	*Journal of Materials Chemistry A*
Manuscript ID	TA-ART-06-2020-005594.R1
Article Type:	Paper
Date Submitted by the Author:	22-Jul-2020
Complete List of Authors:	Jia, Dongbo; Hebei University of Technology Han, Lili; University of California Irvine, Department of Physics Li, Ying; Hebei University of Technology, School of Material Science and Engineering He, Wenjun; Hebei University of Technology Liu, Caichi; Hebei University of Technology, Zhang, Jun; Hebei University of Technology, School of Material Science and Engineering Chen, Cong; Hebei University of Technology Liu, Hui; Hebei University of Technology, Xin, Huolin L.; University of California Irvine, Department of Physics

Journal of Materials Chemistry A

ARTICLE

Optimizing Electron Density of Nickel Sulfides Electrocatalysts through Sulfur Vacancy Engineering for Alkaline Hydrogen Evolution

Received 00th January 20xx,
Accepted 00th January 20xx

DOI: 10.1039/x0xx00000x

www.rsc.org/

Dongbo Jia, [1, a] Lili Han, [2, b] Ying Li, [a] Wenjun He, [a] Caichi Liu, [a] Jun Zhang, [a] Cong Chen, [a] Hui Liu [* a, b] , Huolin L. Xin [*b]

Development of earth-abundant Ni-compound-based electrocatalysts with high performance toward alkaline hydrogen evolution reaction (HER) is of significance for hydrogen generation. Ni_3S_2 catalysts have been widely regarded as a promising candidate, but it suffers from unfavorable hydrogen adsorption characteristics—hydrogen absorption on the Ni sites is not sufficiently strong. Here, by using ab initio calculations, we show that hydrogen adsorption on the Ni sites of Ni_3S_2 catalysts can be tuned by introducing sulfur vacancies. Inspired by this theoretical finding, we fabricate a porous Ni_3S_2 nanosheet array catalyst grown on nickel foam that are rich in sulfur vacancies (Vs-Ni_3S_2/NF) by a plasma-assisted method. The catalyst exhibits a much improved HER activity, which only requires a low overpotential of 88 mV at a current density of 10 mA cm^{-2} and a Tafel slope of 87 mV dec^{-1} in 1 M KOH. This catalyst also shows high durability, which can sustain 15 h of high current density (~ 100 mA cm^{-2}) operation with neglectable degradation. The theoretical and experimental results reveal that the increase in the electron density of Ni sites induced by sulfur vacancies plays a key role in improving its intrinsic activity. This work opens a new direction for rational design of highly efficient transition-metal-compound electrocatalysts toward HER and beyond through defect engineering.

Introduction

With the rapid development of the clean energy, such as solar energy and wind energy, the conversion or storage of these clean power into hydrogen energy through electrochemical water splitting has been regarded as a promising approach.[1, 2] Despite many advantages such as high purity, abundant raw material (H_2O) and zero-carbon emission, alkaline water electrolysis to generate H_2 only occupies about 4% amount in the current industrial market, which is far less than that generated by methane reforming and coal gasification (above 90%).[3] The key factor in impeding the development of alkaline water electrolysis is the high overpotential during the cathodic hydrogen evolution reaction (HER).[4, 5] In order to reduce the high energy consumption, development of highly-efficient HER electrocatalysts is inevitable. Currently, Pt-based materials are still considered as the state-of-the-art catalysts during HER, but the high cost and the scarcity restrict its large-scale application. Therefore, developing non-precious metal-based HER catalysts with high catalytic activity and excellent durability in alkaline medium is urgent, but still of a great challenge.

Over the past few decades, Ni has been widely used in the industrial water electrolysis due to its low cost and strongly alkali resistance.[6-9] However, the HER activity of Ni catalysts remains unsatisfactory because of its strong interaction between the adsorbed H (H*) and the Ni site, which also means a very negative Gibbs free energy of H* (ΔG_{H*}), leading to the difficult desorption of H* from the Ni sites to form H_2.[10, 11] In order to furtheroptimize the Ni-H bond, combining metal Ni with non-metal elements with strong electronegativity such as S, Se, P or N etc to form nickel-based chalcogenides,[12, 13] phosphides[14, 15] and nitrides[16] has been demonstrated as an efficient strategy, which is mainly attributed to the optimized electronic densities of Ni sites influenced by the coordinated S, Se, P or N atoms.[4, 17] Especially, Ni_3S_2 has attracted great interest due to its metal conductivity and excellent stability in recent years.[18-21] Many studies[11, 22-24] indicate the ΔG_{H*} on Ni sites of Ni_3S_2 is more positive than that on Ni sites of metal nickel, which could effectively weaken the Ni-H bond and make the desorption of H* from Ni sites easier. However, too positive ΔG_{H*} makes the hydrogen adsorption difficult, which is also not beneficial for HER.[24-26] Therefore, further optimization of the ΔG_{H*} of Ni_3S_2 through modulating the electronic structure of Ni sites is necessary but still challenging.

The electron densities of transition-metal atom in transition-metal compounds are affected by the type and amount of the coordinated atoms.[27, 28] Hence, both heteroatomic doping and vacancy engineering could effectively tune the electron densities of transition-metal sites, which has been demonstrated by many reported studies.[29-32] However, for the former, the introduction of the heteroatom into a nano-sized

---

[a] School of Material Science and Engineering, Hebei University of Technology, Dingzigu Road 1, Tianjin 300130, P. R. China.

[b] Department of Physics and Astronomy, University of California, Irvine, CA 92697, USA.

†Electronic supplementary information (ESI) available. See DOI: 10.1039/x0xx00000x

compounds without generation of any second phase or defect is not easy to achieve, which makes the revelation of the structure-properties relationship difficult.[33-35] For the latter, vacancy engineering owns many advantages such as clear composition structure, controllable electronic structure and more exposed active sites.[36-39] Recently, the vacancy engineering strategy has been successfully applied in many transition-metal compounds such as cobalt based oxides,[40] nickel oxides,[41] nickel-iron oxyhydroxides,[42] molybdenum disulfides,[43] cobalt sulfides[32] and cobalt selenides[44] catalysts toward HER. Hence, we believe the vacancy engineering strategy may be also effective for Ni_3S_2. To our best knowledge, the vacancy engineering strategy on Ni_3S_2 catalysts toward alkaline HER has been seldom reported.

In order to validate our assumption, we first use density functional theory (DFT) calculation to assess the change of the electronic structure and ΔG_{H*} on the Ni sites of Ni_3S_2 with or without S vacancies, and the ΔG_{H*} of Ni_3S_2 with S vacancies exhibits an optimized value, which is closer to zero eV. Inspired by the theoretical findings, we successfully fabricated a porous Ni_3S_2 nanosheet array catalyst vertically grown on Ni foam that is rich in S vacancies (Vs-Ni_3S_2/NF) by an Ar plasma-assisted process. The obtained Vs-Ni_3S_2/NF catalyst only requires a low overpotential of 88 mV to reach a density current of 10 mA cm^{-2} and a Tafel slope of 87 mV dec^{-1} toward HER in 1 M KOH solution, which is much better than Ni_3S_2/NF catalysts without S vacancies (158 mV@10 mA cm^{-2}, 131 mV dec^{-1}). The advanced structure analysis such as synchrotron-assisted X-ray absorption fine structure (XAFS) and electron paramagnetic resonance (EPR) reveal the existence of the S vacancies in Vs-Ni_3S_2/NF, and tune the electron density of Ni sites, which is consistent with the DFT result.

Experimental

Materials

$Ni(NO_3)_2\cdot 6H_2O$, NH_4F and urea were purchased from Macklin. KOH and ethanol was purchased from Tianjin Chemical Corporation. 2-Mercaptoethanol (99%) was purchased from Sigma. 5 wt% Nafion and 20 wt% Pt/C were purchased from Sigma-Aldrich. All the aforementioned chemicals were used as received without further treatment. Nickel foam (NF, 95% purity) was purchased from Alfa Aesar. Deionized water (DIW, 0.75 µS cm^{-1}) used throughout all experiments was purified through a Millipore system. The NF need to ultrasonic cleaning by acetone, HCl, ethanol and DIW, sequentially. Then dried at 60 °C under vacuum for 8 h.

Synthesis of $Ni(OH)_2$/NF

Typically, $Ni(NO_3)_2\cdot 6H_2O$ (2 mmol), NH_4F (4 mmol) and urea (10 mmol) were dissolved in DIW (40 mL) under stirring for 30 min to obtain homogeneous solution. Subsequently, aforementioned solution and a piece of NF (1 cm × 3 cm) were transferred into an autoclave and heated at 120 °C for 6 h. The $Ni(OH)_2$ nanosheet arrays directly grown on NF ($Ni(OH)_2$/NF) was taken out and washed with DIW for several times, followed by drying at 60 °C for 8 h under vacuum.

Synthesis of Ni_3S_2/NF

2-Mercaptoethanol (2.5 mL) was dissolved in ethanol (25 mL) under stirring for 30 min to obtain a uniform solution. Subsequently, the uniform solution and a piece of dried $Ni(OH)_2$/NF were transferred into an autoclave and heated at 150 °C for 5 h. Finally, the Ni_3S_2/NF was taken out and washed with ethanol for several times, followed by drying under vacuum at 60 °C for 8 h.

Synthesis of Ni_3S_2/NF with sulfur vacancies. (Vs-Ni_3S_2/NF).

In order to obtain Vs-Ni_3S_2/NF, Ar plasma (commercial 3 MHz RF source) with power of 30 W and pressure of 80 Pa and gas flow rate of 300 mL min^{-1} is used to treat the Ni_3S_2/NF precursor with different irradiation time (150, 300, and 600 s). The molar concentration of S vacancies in Vs-Ni_3S_2/NF is defined as x%= (1-n(S)/(n(Ni) × 2/3)) × 100%, where n(S) and n(Ni) represents the molar amount of the S and Ni element, respectively.

Characterizations

X-ray diffraction (XRD) results were obtained through Rigaku DMax-γA diffractometer equipped with Cu Kα radiation (λ =1.5406 Å). Scanning electron microscopy (SEM) and Energy Dispersive Spectrometer (EDS) were performed on FEI Quanta-450 FEG. Low-magnification transmission electron microscopy (TEM) and high resolution TEM (HRTEM) images were acquired on JEM-2010. X-ray Photoelectron Spectrum (XPS) were tested on an Thermo ESCALAB 250XI. X-Ray Absorption Spectroscopy (XAS) measurements were processed on Beamline 8-ID at Brookhaven National Laboratory in which National Synchrotron Light Source with Si (111) monochromator and Lytle detector. Inductively Coupled Plasma-Atomic Emission Spectrometry (ICP-AES) was carried out on a Varian 710-ES. The EDS, XAS and ICP-AES test was performed on Vs-Ni_3S_2 nanosheets peeled off from Ni foam by sonication.

Electrocatalytic Measurements

The electrochemical measurements were assessed on an CHI604E electrochemical workstation equipped with a three-electrode cell. Vs-Ni_3S_2/NF and Ni_3S_2/NF of fixed as 1 cm × 1 cm was used as the working electrode, Hg/HgO as the reference electrode in N_2-saturated 1 M KOH, with a graphite rod as the counter electrode. The cyclic voltammetry (CV) scanning, which cycling the potential between -0.6 V and 0.2 V (versus RHE) at a scan rate of 20 mV s^{-1}, to activate the working electrode in the first place. Polarization curves were recorded using linear sweep voltammetry (LSV) with 90% iR-compensation from -0.6 V and 0.2 V (versus RHE) at a sweep rate of 2 mV s^{-1}. Stability tests were performed by cycling the potential between -0.6 V and 0.2 V (versus RHE) at a scan rate of 100 mV s^{-1} for 3000 cycles first, and the final LSV polarization curves were recorded at 2 mV s^{-1}. The long-term stability was tested under a static overpotential of -100 mV for 15 hours. The electrochemical surface area (ECSA) was calculated by the electrochemical double-layer capacitances (C_{dl}), which was evaluated from CV scanning by different rates from 5 mV s^{-1} to 300 mV s^{-1} in the potential range of 0.1-0.2 V (vs. RHE). The electrochemical impedance spectroscopy (EIS) were obtained by applying an a.c. voltage with 5 mV amplitude in a frequency range from 10 mHz to 1 MHz at -200 mV (vs RHE). All potentials were calibrated versus RHE using: E(RHE) = E(Hg/HgO) + 0.0592 × pH + 0.098.

Electrochemical active surface area

The C_{dl} was converted into electrochemical active surface area (ECSA) using the specific capacitance value of a standard 1 cm^{-2} flat surface which is normally between 20-60 μF cm^{-2}. Therefore, in the following calculation we assume 40 μF cm^{-2} and use 20 and 60 μF cm^{-2} for a lower and upper limit: ECSA = C_{dl} of catalyst (mF cm^{-2})/0.04 mF cm^{-2}.[30, 45] Specific activity of catalyst is obtained from the current density (j) by ECSA value normalizing: j_{ECSA} = j/ECSA.[46]

Turnover frequency

The turnover frequency (TOF) was calculated using the previously reported calculation method:[47, 48]

$$\mathrm{TOF}=\frac{\left(3.12\times10^{15}\frac{\mathrm{H_2/s}}{\mathrm{cm^2}}\mathrm{per}\frac{\mathrm{mA}}{\mathrm{cm^2}}\right)\times|\mathrm{j}|}{\text{Number of active sites}\times\mathrm{ECSA}}$$

where j is the current density, the number of active sites was estimated as the amount of surface sites (including Ni and S atoms).

Theroetical Calculations

Self-consistent total energy calculations are performed based on the projected augmented wave[49] (PAW) method within the Perdew-Burke-Ernzerhof (PBE), as implemented in the Vienna Ab-initio Simulation Package[50, 51] (VASP). Planewave basis sets with a kinetic energy cutoff of 400 eV is used and Monkhorst-Pack grids[52] are set to be 5 × 5 × 1 for all the energy calculations. All structures are fully relaxed until the maximum force on atom is less than 0.02 eV $Å^{-1}$ and the total energy convergence criterion of self-consistent calculation is 10^{-5} eV. The (100) and (110) surfaces of Ni_3S_2 with 15 Å vacuum are used to simulate the catalytic interface. The Gibbs free energy change of H adsorption state is defined as:

$$\Delta G_{H^*}=\Delta E_H+\Delta E_{ZPE}-T\Delta S_H$$

where ΔE_H is the calculated adsorption energy of hydrogen, ΔE_{ZPE} is the difference corresponding to the zero point energy between the adsorbed state and the gas phase, ΔS_H denotes the entropy change.

Results and discussion

Theoretical analysis

DFT calculation was first utilized to identify the electronic structure and intrinsic HER activity of Ni_3S_2/NF and Vs-Ni_3S_2/NF. Based on many previous reports,[24, 53, 54] we took into account the low-index surfaces of (100), (110) and (101) as the simulated models, since these surfaces had low surface energies and might be easily exposed. The calculated formation energies of the surface S vacancies in the three models indicate that the formation energy of S vacancies at (101) surface sites (3.639 eV) is obviously larger than those at (100) surfaces sites (2.223 eV) and (110) surfaces sites (2.745 eV), implying that the formation of S vacancies at (101) surfaces is harder than that at (100) and (110) surfaces, so we choose (100) and (110) surfaces as the simulated models. Furthermore, for (100) and (110) models, the formation energies of S vacancy at the inner lattice sites are also obviously larger than that at the surface sites (**Table S1**), demonstrating that the S vacancies prefers the surfaces sites. Hence, only surface S vacancies at (100)-terminated and (110)-terminated are considered here, as shown in the simulated models of Ni_3S_2 and Vs-Ni_3S_2 of **Figure S1**. To gain a deep insight into the effect of S vacancy on the electronic densities of neighboring Ni atoms, we calculated the differential charge densities of Ni_3S_2 and Vs-Ni_3S_2, as illustrated in **Figure 1a** and **1b**. Whether on (100) or (110) surfaces, the localized electron densities of Ni atom around the S vacancies of Vs-Ni_3S_2 are larger than that of the pristine Ni_3S_2, which may be attributed to the contribution of the localized electrons left by the removed S atoms.[37, 55] This result is further supported by the Bader charge analysis, as shown in **Figure S2**. The changed electron densities of Ni site will influence the d-band center (ε_d) considered as an useful descriptor to evaluate the intrinsic HER activity of the transition-metal-based catalysts.[56, 57] The more positive the ε_d becomes, the stronger bonding between the adsorbate and the active sites will be, which is ascribed to the reduced filling of antibonding orbital states.[58, 59] As shown in **Figure 1c** and **1d**, the ε_d values of Vs-Ni_3S_2 for both (100) and (110)-terminated facets calculated by the projected density of states (DOS) shift positively toward Fermi level compared to those of the pristine Ni_3S_2, thus strengthening the hydrogen adsorption on the Ni sites.[60] According to the calculated ε_d results, we believe that Vs-Ni_3S_2 with strong Ni-H bonds should have high HER activity.[24]

To further discuss the effect of the changed electronic structure of Vs-Ni_3S_2 on their HER performance, we calculated the ΔG_{H^*} of Ni_3S_2 and Vs-Ni_3S_2 on different active sites including Ni, S and S vacancies, respectively. For an ideal HER catalyst, the ΔG_{H^*} should be zero eV, implying that the bonding between the adsorbate and the active site is neither strong nor weak, which is also so-called Sabatier principle.[61, 62] As illustrated in **Figure 1e** and **1f**, whether (100) or (110) surfaces for the pristine Ni_3S_2, the ΔG_{H^*} on the nickel sites are much larger than zero eV, implying a relatively weak bonding between hydrogen atom and nickel sites, and the sulfur sites will be better H-adsorbed sites since the ΔG_{H^*} on them are closer to zero eV. After the introduction of S vacancies into the Ni_3S_2, the ΔG_{H^*} on Ni sites for (100) and (110) surfaces are optimized to 0.217 and 0.613 eV, respectively, which are closest to the promising ΔG_{H^*} among all possible sites including Ni, S and S-vacancies sites, indicating that the Ni sites turn into the best H-adsorbed sites. The reduced ΔG_{H^*} on Ni sites of (100) and (110) surfaces for Vs-Ni_3S_2 also means an enhanced Ni-H interaction and an improved intrinsic HER activity, agreeing well with the differential charge densities and d-band center analysis. For further discussing the effect of vacancy concentrations on the hydrogen adsorption energies, the ΔG_{H*} of Vs-Ni_3S_2 with different S vacancy concentrations ranged from 5% to 15% (atomic ratio) were calculated, as shown in **Figure S3.** It can be observed that the ΔG_{H*} will decrease with increasing the S vacancy concentrations, implying the strengthened bonding between the active sites and hydrogen atom, and the moderate S vacancy concentration (10%) exhibits the optimal hydrogen adsorption energy. In addition, the dissociation of water is also an important process during alkaline HER.[63] As illustrated in **Figure S4**, the energy barriers of water dissociation for Vs-Ni_3S_2 are smaller than those for Ni_3S_2, which are also beneficial for accelerating HER process. In a word, all discussions aforementioned demonstrate the intrinsic activity of Vs-Ni_3S_2 catalysts toward HER is better than that of Ni_3S_2 catalysts.

Figure 1. (a, b) The differential charge densities of the (100) and (110) surfaces for Ni_3S_2 and Vs-Ni_3S_2 (yellow and blue regions represent electron accumulation and depletion, respectively), (c, d) the projected electronic densities of states of the d-band for the Ni atoms on the (100) and (110) surface of Ni_3S_2 and Vs-Ni_3S_2 (the horizontal dashed lines indicate the calculated d-band center), (e, f) Gibbs free energies of H adsorption, ΔG_{H*}, on different sites of the (100) and (110) surfaces for Ni_3S_2 and Vs-Ni_3S_2.

Microstructure analysis

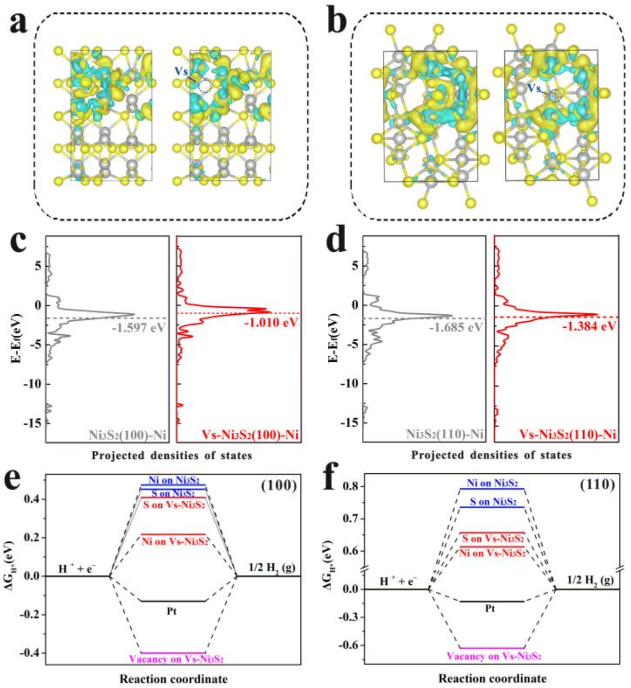

Inspired by the DFT results, we synthesized a Ni_3S_2/NF catalyst with S vacancies through Ar plasma etching process. First, Ni_3S_2 nanosheet arrays grown on Ni foam (Ni_3S_2/NF) were obtained via the hydrothermal sulfurization of $Ni(OH)_2$/NF nanosheet arrays according to the previous process.[21, 26] Then, the as-prepared Ni_3S_2/NF was exposed to an Ar plasma atmosphere for introduction of S vacancies, and the amount of S vacancies could be controlled by varying the plasma operation times (150, 300 and 600 s), as shown in **Figure 2a**. The detailed process was illustrated in the experimental section. To identify the phase structure of the products, X-ray diffraction (XRD) was performed, as shown in **Figure 2b**. It can be observed that all peaks except the three strong peaks belonged to Ni (JCPDS 04-0850) are assigned to the hexagonal heazlewoodite Ni_3S_2 (JCPDS 44-1418), indicating that the Ar plasma etching has no obvious effect on the phase structure of the materials. Scanning electron microscopy (SEM) and transmission electron microscopy (TEM) were used to characterize the morphology structure of the as-obtained samples. As seen in **Figure 3a**, **3b** and **3e**, the as-prepared Ni_3S_2/NF was composed of numerous nanosheets vertically grown on NF with an average thickness of ~85 nm, and the nanosheet is assembled by small nanoparticles. After Ar-plasma treatment for different times, we can observe numerous pores in the Vs-Ni_3S_2/NF products (**Figure 3c**, **3d**, **3f** and **Figure S5**), leading to larger Brunauer-Emmett-Teller (BET) surface area (3.44 $m^2\ g^{-1}$) than the pristine Ni_3S_2/NF (1.59 $m^2\ g^{-1}$) as shown in **Figure S6**, which may be beneficial for increasing the active sites numbers. The average size for Vs-Ni_3S_2/NF nanoparticles are 37.63 nm (**Figure S7**), which is almost equal to the pristine Ni_3S_2/NF (37.92 nm), effectively excluding the influence of the size effect on the HER performance.[32] Take one typical Vs-Ni_3S_2 nanoplate treated for 300 s (Vs-Ni_3S_2/NF-300) as an example, the clear lattice fringes with distances of 0.23 and 0.24 nm are corresponding to (021) and (003) planes of hexagonal Ni_3S_2, respectively (**Figure 3g**). The relative Fast Fourier Transform (FFT) pattern indicates that the HRTEM image is obtained along [100] crystal orientation.[12, 26] Another HRTEM image of the edge of Vs-Ni_3S_2/NF nanoplate (**Figure S8**) displays the uneven surface and the appearance of (300) and (110) facets with distances of 0.17 and 0.29 nm, respectively, which is consistent with the simulated models. Moreover, the amount of S vacancies in Vs-Ni_3S_2/NF treated with different times were also characterized by the Energy Dispersive Spectroscopy (EDS) and Inductively Coupled Plasma-Atomic Emission Spectrometry (ICP-AES), which are shown in **Figure S9** and **Table S2**. The molar fractions of S vacancies in Vs-Ni_3S_2/NF treated for 150 s, 300 s and 600 s are 3.93 %, 7.18 % and 11.63 % measured by EDS, respectively, which are close to the values by ICP-AES (4.46 %, 8.54 % and 12.78 %).

Figure 2. (a) The schematic illustration for the preparation of Vs-Ni_3S_2/NF by Ar plasma etching, (b) XRD patterns of Ni_3S_2/NF and Vs-Ni_3S_2/NF treated with different plasma etching times of 150, 300 and 600 s, respectively.

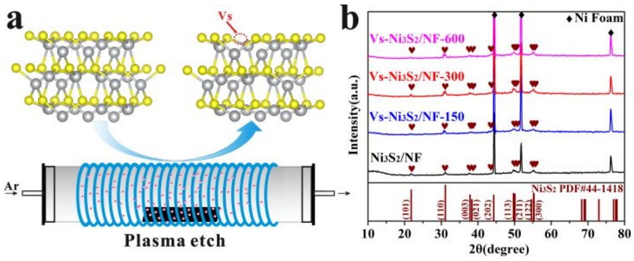

Figure 3. SEM images of (a, b) Ni_3S_2/NF and (c, d) Vs-Ni_3S_2/NF-300, TEM images of (e) Ni_3S_2/NF and (f) Vs-Ni_3S_2/NF-300, (g) HRTEM image of Vs-Ni_3S_2/NF-300.

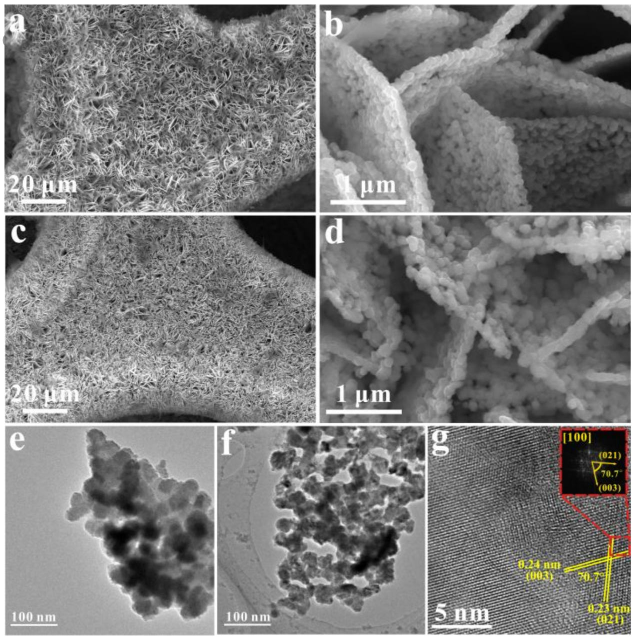

To further demonstrate the existence of S vacancies in the Vs-Ni_3S_2/NF products, the synchrotron-based X-ray absorption fine structure (XAFS) spectroscopy tests was performed. Ni K-edge extend X-ray absorption fine structure (EXAFS) and Fourier transform (FT) of K^3-weighted Ni EXAFS spectra for Vs-Ni_3S_2 and Ni_3S_2 nanosheets were illustrated in **Figure S10a** and **Figure 4a**, respectively. The strong peak located at ~ 1.81 Å for Vs-Ni_3S_2/NF and Ni_3S_2/NF is assigned to the nearest Ni-S bond in the first coordination shell.[64, 65] Obviously, the Ni-S bond intensity of Vs-Ni_3S_2/NF is weaker than that of Ni_3S_2/NF, implying the reduced S coordination number of Ni site, which is attributed to the formation of pores and S vacancies.[32] The enhanced Ni-Ni bond intensity (~ 2.93 Å) also confirms the existence of S vacancies in Vs-Ni_3S_2/NF. The oscillation curves of Vs-Ni_3S_2 at the k range of 0-12 Å^{-1} is similar with that of Ni_3S_2/NF, suggesting the same phase structure for them (**Figure S10b**), but the reduced intensity of Vs-Ni_3S_2/NF relative to that of Ni_3S_2/NF is ascribed to the S vacancies.[31, 66] Moreover, the absorption edge of Ni K-edge X-ray absorption near edge structure (XANES) shown in **Figure 4b** clearly indicates that the chemical valence of Ni in Vs-Ni_3S_2/NF is lower than that in Ni_3S_2/NF, agreeing well with DFT calculation result (**Figure 1a** and **1b**), which also supports the existence of S vacancies in Vs-Ni_3S_2/NF. To further confirm the XAFS results, we carried out the electron paramagnetic resonance (EPR), as shown in **Figure 4c**. The Vs-Ni_3S_2/NF sample has an obviously stronger resonance EPR signal with g = 2.003 than Ni_3S_2/NF, which is corresponding to S vacancies.[32, 67] The X-ray photoelectron spectroscopy (XPS) measurement was also performed (**Figure 4d** and **Figure S11**). For Ni 2p spectra, compared with the pristine Ni_3S_2/NF, the Ni $2p_{3/2}$ (855.2 eV) and Ni $2p_{1/2}$ (873.0 eV) peaks belonged to Ni-S bond of Vs-Ni_3S_2/NF shift negatively, demonstrating a lower chemical valence of Ni in Vs-Ni_3S_2/NF, which is also attributed to the S vacancies and consistent with the DFT calculation and XAFS results.[32]

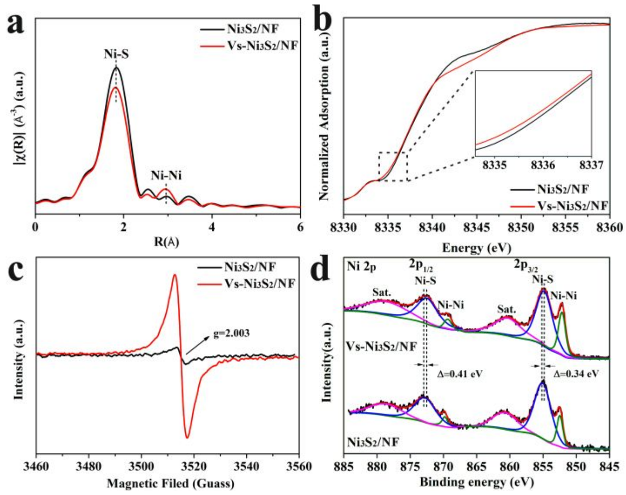

Figure 4. (a) Magnitude of K^3-weighted Fourier transforms of Ni K-edge EXAFS spectra for Ni_3S_2/NF and Vs-Ni_3S_2/NF, (b) Ni K-edge XANES spectra, (c) EPR spectra of Ni_3S_2/NF and Vs-Ni_3S_2/NF, (d) XPS spectra of Ni 2p for Ni_3S_2/NF and Vs-Ni_3S_2/NF.

Electrocatalytic performance analysis.

In order to evaluate the HER performance of the Vs-Ni_3S_2/NF electrode, the electrochemical measurements were carried out in 1 M KOH. For comparison, the bare NF, Ni_3S_2/NF, Vs-Ni_3S_2/NF and Pt/C (20 wt %) on NF (Pt/C/NF) electrodes were also tested, and the loading amount of the catalysts on NF were shown in **Table S3**. **Figure 5a** displays the linear sweep voltammetry (LSV) curves of the as-prepared electrodes. The Vs-Ni_3S_2/NF treated for 300 s (Vs-Ni_3S_2/NF-300) electrode exhibits an excellent alkaline HER activity, only requiring 88,

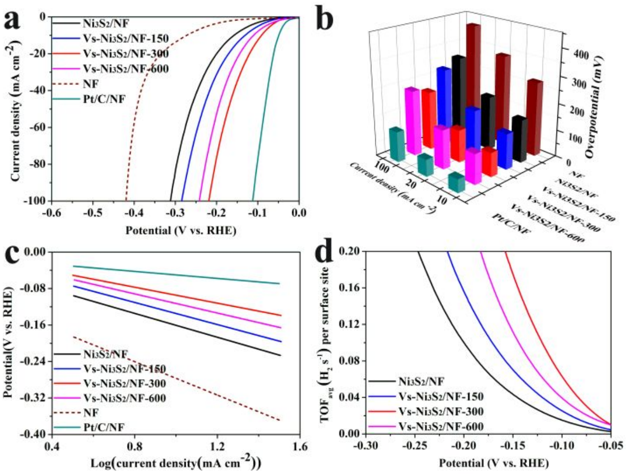

Figure 5. (a) LSV curves of the HER performance of NF, Pt/C/NF, Ni_3S_2/NF and Vs-Ni_3S_2/NF treated with different times, (b) comparison of overpotentials at 10, 20, and 100 mA cm^{-2}, (c) Tafel plots derived from (a), (d) the potential-dependent TOF curves of the Ni_3S_2/NF and Vs-Ni_3S_2/NF treated with different time.

120 and 218 mV to deliver a current density of 10, 20 and 100 mA cm^{-2}, which is better than NF (274, 336 and 420 mV), Ni_3S_2/NF (158, 200 and 312 mV), Vs-Ni_3S_2/NF-150 (131, 170 and 284 mV) and Vs-Ni_3S_2/NF-600 (110, 144 and 242 mV), as shown in **Figure 5b**. Especially, the electrocatalytic activity of the Vs-Ni_3S_2/NF-300 electrode toward alkaline HER is superior or comparable to most of the non-precious transition-metal compounds catalysts recently reported (**Table S4**). Moreover, **Figure 5c** shows that the Tafel slope of the Vs-Ni_3S_2/NF-300 electrode (87 mV dec^{-1}) is smaller than that of Ni_3S_2/NF (131 mV dec^{-1}), Vs-Ni_3S_2/NF-150 (121 mV dec^{-1}) and Vs-Ni_3S_2/NF-600 (105 mV dec^{-1}), also implying a faster reaction kinetics. Moreover, the turnover frequency (TOF) was also utilized to evaluate the intrinsic activity of the as-prepared electrodes, and the TOF values of Vs-Ni_3S_2/NF-300 electrode are significantly larger than those of Ni_3S_2/NF, Vs-Ni_3S_2/NF-150 and Vs-Ni_3S_2/NF-600, (**Figure 5d**), indicating its better intrinsic HER activity, which confirms the prediction of DFT calculation results (**Figure 1**).

To further study the reasons for the high HER activity of the Vs-Ni_3S_2/NF-300 electrodes, we assessed the electrochemically active surface areas (ECSA) of the as-prepared electrodes by measuring the electrochemical double-layer capacitances (C_{dl}) (**Figure 6a** and **Figure S12**). The ECSA of Vs-Ni_3S_2/NF-300 are about 0.99, which is larger than Ni_3S_2/NF (0.46), Vs-Ni_3S_2/NF-150 (0.68) and Vs-Ni_3S_2/NF-600 (0.83), suggesting a more active sites of Vs-Ni_3S_2/NF-300 due to the existence of numerous pores and S vacancies. For gaining an insight into the HER kinetics of the electrodes, electrochemical impedance spectroscopy (EIS) was also carried out. **Figure 6b** displays the Nyquist plots with an equivalent circuit for the electrodes, and the Vs-Ni_3S_2/NF-300 has the smallest R_{ct} value among all electrodes (**Table S5**), indicating the fastest charge-transfer property between the electrode and electrolyte during HER. Moreover, to exclude the contribution of the increased active site numbers, the LSV curves of the electrodes normalized by ECSA and BET surfaces were also plotted in **Figure 6c and Figure S13**. Interestingly, the specific activities of Vs-Ni_3S_2/NF-300 electrode normalized by either ECSA or BET are still superior to that of Ni_3S_2/NF, Vs-Ni_3S_2/NF-150 and Vs-Ni_3S_2/NF-600, implying a better intrinsic activity, which is consistent with the DFT calculation (**Figure S3**) and TOF results (**Figure 5d**).

Besides the high catalytic activity, the excellent durability is also a key parameter to evaluate an idea catalyst. **Figure 6d** exhibits the LSV curve of Vs-Ni_3S_2/NF-300 measured after 3000 CV cycles. It can be observed that the overpotential at 100 mA cm^{-2} only increases by 3 mV, indicating the excellent stability of the Vs-Ni_3S_2/NF-300 electrode during HER in 1 M KOH. Moreover, the long-term durability of the Vs-Ni_3S_2/NF-300 electrode was also tested under a large overpotential of -240 mV (vs RHE) for 15 hours (insert of **Figure 6d**). The HER current density of the Vs-Ni_3S_2/NF-300 electrode only reduced 4.1%, implying its superior long-term durability. Additionally, the structure stability of Vs-Ni_3S_2/NF after 15 h durability test was also discussed by XRD, XPS, EDS, SEM and TEM measurements, as shown in **Figure S14** and **Figure S15**. It is obvious that the phase structure, chemical states, stoichiometric ratio and micro-morphology of Vs-Ni_3S_2/NF after the stability test remain almost unchanged. But the O content in Vs-Ni_3S_2/NF-300 has slight increase, possibly ascribing to the the chemical adsorption of oxygen-contained species formed during the HER in alkaline electrolyte, which is very common in many reported transition-metal nonoxide electrocatalysts.[68, 69] Furthermore, **Figure S16** reveals that the faradaic efficiency is close to 100% on Vs-Ni_3S_2/NF electrode in alkaline media.

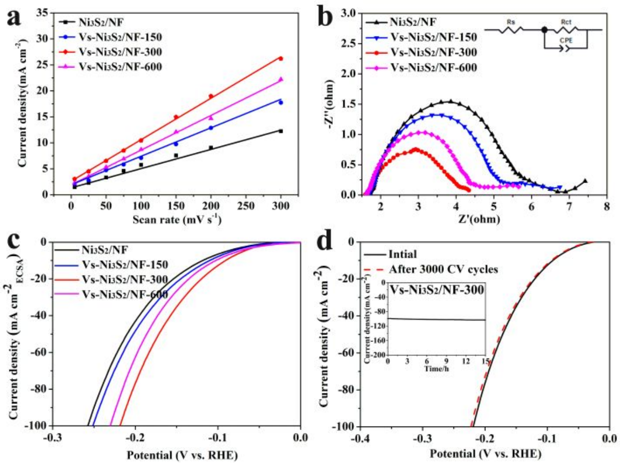

Figure 6. (a) Calculated electrochemical double-layer capacitance Ni_3S_2/NF and Vs-Ni_3S_2/NF treated with different time, (b) Nyquist plots of Ni_3S_2/NF and Vs-Ni_3S_2/NF treated with different time, (c) specific activity of Ni_3S_2/NF and Vs-Ni_3S_2/NF treated with different time based on ECSA, (d) LSV curves of Vs-Ni_3S_2/NF-300 after the 1st and 3000th CV cycles [inset: long-term stability test of Vs-Ni_3S_2/NF-300 at -240 mV (vs RHE)].

Conclusions

In summary, we theoretically predicted that the introduction of S vacancies into Ni_3S_2 could effectively enhance the intrinsic activity of Ni_3S_2 catalysts toward alkaline HER, and then the experiments successfully validated this prediction. The as-prepared Ni_3S_2 nanosheet arrays with optimized S vacancies concentrations exhibited excellent HER performance, only needing a low overpotential of 88 mV and a Tafel slope of 87 mV dec^{-1} at 10 mA cm^{-2} in 1 M KOH, which was much better than that of the pristine Ni_3S_2 nanosheet arrays (158 mV@10 mA cm^{-2}). Moreover, both the theoretical calculation and experiment results confirm that the S vacancies in Ni_3S_2 increases the electron densities of Ni sites, resulting in optimized hydrogen adsorption energy and accelerated water dissociation. This methodology of optimizing the electron densities of transition-metal sites through combing anion vacancies (sulphur, selenium, phosphorus or nitrogen vacancies) would be a widespread way to improve the HER catalytic activity of transition-metal compounds beyond Ni_3S_2.

Conflicts of interest

There are no conflicts to declare.

Author contributions

Dongbo Jia and Lili Han contributed equally to this work.

Corresponding Authors

* E-mail: liuhuihebut@163.com

* E-mail: huolin.xin@uci.edu

Acknowledgements

The authors gratefully acknowledge the financial support from Nature Science Foundation of Hebei Province (E2019202206) and National Natural Science Foundation of China (No. 51402085).

References

1. Turner, J. A., *Science*, 1999, **285**, 687-689.
2. Z. W. Seh, J. Kibsgaard, C. F. Dickens, I. B. Chorkendorff, J. K. Norskov and T. F. Jaramillo, *Science*, 2017, **355,** eaad4998.
3. X. Zou and Y. Zhang, *Chem Soc. Rev.*, 2015, **44**, 5148-5180.
4. Y. Zheng, Y. Jiao, A. Vasileff and S. Z. Qiao, *Angew. Chem. Int. Edit.*, 2018, **57**, 7568-7579.
5. J. Zhu, L. Hu, P. Zhao, L. Y. S. Lee and K. Y. Wong, *Chem. Rev.*, 2020, **120**, 851-918.
6. L. Ji, C. Lv, Z. Chen, Z. Huang and C. Zhang, *Adv. Mater.*, 2018, **30,** 1705653.
7. V. Vij, S. Sultan, A. M. Harzandi, A. Meena, J. N. Tiwari, W. G. Lee, T. Yoon and K. S. Kim, *ACS Catal.*, 2017, **7**, 7196-7225.
8. X. Yan, M. Gu, Y. Wang, L. Xu, Y. Tang and R. Wu, *Nano Res.*, 2020, **13**, 975-982.
9. X. Wu, T. Zhang, J. Wei, P. Feng, X. Yan and Y. Tang, *Nano Res.*, 2020, DOI: 10.1007/s12274-020-2819-4.
10. Y. Li, Y. Sun, Y. Qin, W. Zhang, L. Wang, M. Luo, H. Yang and S. Guo, *Adv. Energy Mater.*, 2020, **10**, 1903120.
11. J. K. Norskov, T. Bligaard, A. Logadottir, J. R. Kitchin, J. G. Chen, S. Pandelov and J. K. Norskov, *J. Electrochem. Soc.*, 2005, **152**, J23-J26.
12. S. Deng, K. Zhang, D. Xie, Y. Zhang, Y. Zhang, Y. Wang, J. Wu, X. Wang, J. Fan Hong, X. Xia and J. Tu, *Nano-Micro Lett.*, 2019, **11,** 205-216.
13. D. Kong, J. J. Cha, H. Wang, H. R. Lee and Y. Cui, *Energy Environ. Sci.,* 2013, **6**, 3553-3558.
14. B. You, N. Jiang, M. L. Sheng, M. W. Bhushan and Y. J. Sun, *ACS Catal.*, 2016, **6**, 714-721.
15. C. C. Liu, T. Gong, J. Zhang, X. Zheng, J. Mao, H. Liu, Y. Li and Q. Hao, *Appl. Catal. B*, 2020, **262**, 118245.
16. B. Liu, B. He, H. Q. Peng, Y. Zhao, J. Cheng, J. Xia, J. Shen, T. W. Ng, X. Meng, C. S. Lee and W. Zhang, *Adv. Sci.*, 2018, **5,** 1800406.
17. C. Hu, L. Zhang and J. Gong, *Energy Environ. Sci.*, 2019, **12**, 2620-2645.
18. N. Jiang, Q. Tang, M. Sheng, B. You, D. E. Jiang and Y. Sun, *Catal. Sci. Technol.*, 2016, **6**, 1077-1084.
19. W. Zhou, X. J. Wu, X. Cao, X. Huang, C. Tan, J. Tian, H. Liu, J. Wang and H. Zhang, *Energy Environ. Sci.*, 2013, **6**, 2921-2924.
20. W. J. He, L. L. Han, Q. Y. Hao, X. R. Zheng, Y. Li, J. Zhang, C. C. Liu, H. Liu and H. L. Xin, *ACS Energy Lett.*, 2019, **4**, 2905-2912.
21. C. C. Liu, D. B. Jia, Q. Y. Hao, X. R. Zheng, Y. Li, C. C. Tang, H. Liu, J. Zhang and X. L. Zheng, *ACS Appl. Mater. Inter.*, 2019, **11**, 27667-27676.
22. J. Dong, F. Q. Zhang, Y. Yang, Y.-B. Zhang, H. He, X. Huang, X. Fan and X. M. Zhang, *Appl. Catal. B,* 2019, **243**, 693-702.
23. L. Li, C. Sun, B. Shang, Q. Li, J. Lei, N. Li and F. Pan, *J. Mater. Chem. A*, 2019, **7**, 18003-18011.
24. T. Kou, T. Smart, B. Yao, I. Chen, D. Thota, Y. Ping and Y. Li, *Adv. Energy Mater.*, 2018, **8,** 1703538.
25. P. Chen, T. Zhou, M. Zhang, Y. Tong, C. Zhong, N. Zhang, L. Zhang, C. Wu and Y. Xie, *Adv. Mater.*, 2017, **29,** 1701584.
26. G. Zhang, Y.-S. Feng, W. T. Lu, D. He, C. Y. Wang, Y. K. Li, X.-Y. Wang and F. F. Cao, *ACS Catal.*, 2018, **8**, 5431-5441.
27. H. Li, C. Tsai, A. L. Koh, L. L. Cai, A. W. Contryman, A. H. Fragapane, J. H. Zhao, H. S. Han, H. C. Manoharan, F. Abild-Pedersen, J. K. Norskov and X. L. Zheng, *Nat. Mater.*, 2016, **15**, 48-53.
28. Y. Liu, H. Cheng, M. Lyu, S. Fan, Q. Liu, W. Zhang, Y. Zhi, C. Wang, C. Xiao, S. Wei, B. Ye and Y. Xie, *J. Am. Chem. Soc.*, 2014, **136**, 15670-15675.
29. J. Hao, W. Yang, Z. Peng, C. Zhang, Z. Huang and W. Shi, *ACS Catal.*, 2017, **7**, 4214-4220.
30. Y. Wu, X. Liu, D. Han, X. Song, L. Shi, Y. Song, S. Niu, Y. Xie, J. Cai, S. Wu, J. Kang, J. Zhou, Z. Chen, X. Zheng, X. Xiao and G. Wang, *Nat. Commun.*, 2018, **9,** 1425-1425.
31. Q. He, Y. Wan, H. Jiang, Z. Pan, C. Wu, M. Wang, X. Wu, B. Ye, P. M. Ajayan and L. Song, *ACS Energy Lett.*, 2018, **3**, 1373-1380.
32. C. Zhang, Y. Shi, Y. Yu, Y. Du and B. Zhang, *ACS Catal.*, 2018, **8**, 8077-8083.
33. Y. R. Zheng, P. Wu, M. R. Gao, X. L. Zhang, F. Y. Gao, H. X. Ju, R. Wu, Q. Gao, R. You, W. X. Huang, S. J. Liu, S. W. Hu, J. F. Zhu, Z. Y. Li and S. H. Yu, *Nat. Commun.*, 2018, **9**, 2533.
34. S. Jiang, R. Zhang, H. Liu, Y. Rao, Y. Yu, S. Chen, Q. Yue, Y. Zhang and Y. Kang, *J. Am. Chem. Soc.*, 2020, DOI: 10.1021/jacs.9b13915.
35. J. M. Zhang, X. P. Xu, L. Yang, D. J. Cheng and D. P. Cao, *Small Methods*, 2019, **9,** 1900653.
36. Y. Jia, K. Jiang, H. Wang and X. Yao, *Chem*, 2019, **5**, 1371-1397.
37. C. Tsai, H. Li, S. Park, J. Park, H. S. Han, J. K. Norskov, X. Zheng and F. Abild-Pedersen, *Nat. Commun.*, 2017, **8,** 15113.
38. K. Y. Kim, J. Lee, S. Kang, Y. W. Son, H. W. Jang, Y. Kang and S. Han, *ACS Catal.*, 2018, **8**, 4508-4515.
39. D. Yan, Y. Li, J. Huo, R. Chen, L. Dai and S. Wang, *Adv. Mater.*, 2017, **29,** 1606459.
40. L. Xu, Q. Jiang, Z. Xiao, X. Li, J. Huo, S. Wang and L. Dai, *Angew. Chem. Int. Edit.*, 2016, **55**, 5277-5281.
41. T. Zhang, M. Y. Wu, D. Y. Yan, J. Mao, H. Liu, W. B. Hu, X. W. Du, T. Ling and S. Z. Qiao, *Nano Energy*, 2018, **43**, 103-109.
42. A. Majid, Y. Yichun, L. Yibing, S. Chenghua and Z. Chuan, *ACS Energy Lett.*, 2018, **3,** 1515-1520.
43. H. Li, C. Tsai, A. L. Koh, L. L. Cai, A. W. Contryman, A. H. Fragapane, J. H. Zhao, H. S. Han, H. C. Manoharan, F. Abild-Pedersen, J. K. Norskov and X. L. Zheng, *Nat. Mater.*, 2016, **15**, 48-53.

44. Y. Zhang, C. Zhang, Y. Guo, D. Liu, Y. Yu and B. Zhang, *J. Mater. Chem. A*, 2019, **7**, 2536-2540.
45. R. Zhang, X. X. Wang, S. J. Yu, T. Wen, X. W. Zhu, F. X. Yang, X. N. Sun, X. K. Wang and W. P. Hu, *Adv. Mater.*, 2017, **29**, 1605502.
46. D. Voiry, M. Chhowalla, Y. Gogotsi, N. A. Kotov, Y. Li, R. M. Penner, R. E. Schaak and P. S. Weiss, *ACS Nano*, 2018, **12**, 9635-9638.
47. E. J. Popczun, J. R. McKone, C. G. Read, A. J. Biacchi, A. M. Wiltrout, N. S. Lewis and R. E. Schaak, *J. Am. Chem. Soc.*, 2013, **135**, 9267-9270.
48. H. W. Liang, S. Brueller, R. Dong, J. Zhang, X. Feng and K. Muellen, *Nat. Commun.*, 2015, **6,** 7992.
49. P. E. B. O. Chl, *Phys. Rev. B*, 1994, **50**, 17953-17979.
50. G. Kresse and J. Furthmüller, *Phys. Rev. B*, **54**, 11169-11186.
51. G. Kresse and J. Hafner, *Phys. Rev. B*, 1994, **49**, 14251-14269.
52. Chadi and J. D., *Phys. Rev. B 1976*, **13**, 5188-5192.
53. Y. Yang, H. Yao, Z. Yu, S. M. Islam, H. He, M. Yuan, Y. Yue, K. Xu, W. Hao, G. Sun, H. Li, S. Ma, P. Zapol and M. G. Kanatzidis, *J. Am. Chem. Soc.*, 2019, **141**, 10417-10430.
54. J. X. Feng, J. Q. Wu, Y. X. Tong and G. R. Li, *J. Am. Chem. Soc.*, 2018, **140**, 610-617.
55. X. Wang, Y. Zhang, H. Si, Q. Zhang, J. Wu, L. Gao, X. Wei, Y. Sun, Q. Liao, Z. Zhang, K. Ammarah, L. Gu, Z. Kang and Y. Zhang, *J. Am. Chem. Soc.*, 2020, **142**, 4298-4308.
56. B. Hammer and J. K. Norskov, *Surf. Sci.*, 1996, **343**, 211-220.
57. B. Hammer and J. K. Norskov, *Nature*,1995, **376**, 238-240.
58. H. Xin, A. Vojvodic, J. Voss, J. K. Norskov and F. Abild-Pedersen, *Phys. Rev. B*, 2014, **89**, 115114.
59. Norskov, J. K. , Studt, F., Abildpedersen, F., Bligaard, T. *Angew. Chem., Int. Ed.* **2015,** *54*, 10404-10405.
60. Y. Jiao, Y. Zheng, M. Jaroniec and S. Z. Qiao, *Chem. Soc. Rev.*, 2015, **44**, 2060-2086.
61. M. Che, *Catal. Today*, 2013, **218**, 162-171.
62. A. J. Medford, A. Vojvodic, J. S. Hummelshoj, J. Voss, F. Abild-Pedersen, F. Studt, T. Bligaard, A. Nilsson and J. K. Norskov, *J. Catal.*, 2015, **328**, 36-42.
63. R. Subbaraman, D. Tripkovic, D. Strmcnik, K. C. Chang, M. Uchimura, A. P. Paulikas, V. Stamenkovic and N. M. Markovic, *Science*, 2011, **334**, 1256-1260.
64. J. Yin, J. Jin, H. Zhang, M. Lu, Y. Peng, B. Huang, P. Xi and C. H. Yan, *Angew. Chem. Int. Edit.*, 2019, **58,** 18676-18682.
65. Q. Ma, C. Hu, K. Liu, S. F. Hung, D. Ou, H. M. Chen, G. Fu and N. Zheng, *Nano Energy*, 2017, **41**, 148-153.
66. Y. Wang, Y. Zhang, Z. Liu, C. Xie, S. Feng, D. Liu, M. Shao and S. Wang, *Angew. Chem. Int. Edit.*, 2017, **56**, 5867-5871.
67. Y. Yin, J. Han, Y. Zhang, X. Zhang, P. Xu, Q. Yuan, L. Samad, X. Wang, Y. Wang, Z. Zhang, P. Zhang, X. Cao, B. Song and S. Jin, *J. Am. Chem. Soc.*, 2016, **138**, 7965-7972.
68. B. Song, K. Li, Y. Yin, T. Wu, L. Dang, M. Caban-Acevedo, J. Han, T. Gao, X. Wang, Z. Zhang, J. R. Schmidt, P. Xu and S. Jin, *ACS Catal.,* 2017, **7**, 8549-8557.
69. Y. Zhang, L. Gao, E. J. M. Hensen and J. P. Hofmann, *ACS Energy Lett.*, 2018, **3**, 1360-1365.

Table of Contents

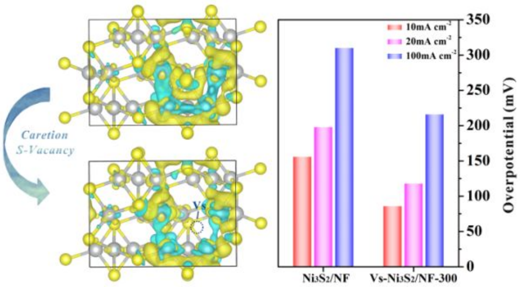

A novel, rational design for porous S-vacancy nickel sulfides catalysts with remarkable catalytic performance for alkaline HER.